Bull Earthquake Eng (2018) 16:1725–1750
https://doi.org/10.1007/s10518-017-0272-x

ORIGINAL RESEARCH PAPER

A reliable computerized litho-morphometric model for development of 3D maps of Topographic Aggravation Factor (TAF): the cases of East Mountain (Utah, USA) and Port au Prince (Haiti)

G. Grelle[1] · C. Wood[2] · L. Bonito[3] · G. Sappa[1] · P. Revellino[3] · S. Rahimi[2] · F. M. Guadagno[3]

Received: 4 March 2017 / Accepted: 28 October 2017 / Published online: 24 November 2017

Abstract A reliability analysis was performed of a model capable of computing Topographic Aggravation Factors (TAF) for real topographic features using a digital elevation model. This model is a module in the SiSeRHMap hybrid model that, by a metamodeling process, computes frequency depending maps (multispectral) of acceleration response taking into account the topographic effect. The model is described by a structure comparable to a series–parallel circuit problem that solves for the response of each given x, y, z map point by scaling the 1D seismic response by the TAF in the frequency domain (each a component of the series circuit). The TAF is dependent on two coupled factors (the parallel components): (1) the 3D shape of the surface and (2) the stiffness of an "equivalent uniform relief". Reliability analyses were performed on two different areas each characterized by complex topographic features. The first case modelled the East Mountain area (Utah, USA), where a detailed topographic effects study was conducted. A comparison between the TAFs developed in this study and the estimated Median Reference Method and Standard Spectral Ratio results calculated from the recorded ground motions indicated good agreement between the numerical and experimental results. The second case performed a comparison-parametric analysis of two nearby topographic features located in Port-au-Prince, Haiti. For this case, the complete SiSeRHMap model was applied by utilizing stratigraphic and topographic modules. The results clearly confirm the role of the 3D-topographic surface in the seismic site response and the reliability of SiSeRHMap in predicting it.

✉ G. Grelle
gerardo.grelle@uniroma1.it

[1] Department of Civil and Environmental Engineering, University of Rome "La Sapienza", Via Eudossiana, 18, 00184 Rome, Italy

[2] Department of Civil Engineering, University of Arkansas, 4190 Bell Engineering Center, Fayetteville, AR 72701, USA

[3] Department of Science and Technologies, University of Sannio, Via Dei Mulini 59/A, 82100 Benevento, Italy

Keywords Topographic effect · Site seismic response · Microzonation · Geographic information system

1 Introduction

Topographic effects can be a significant component of seismic site response typically occurring in areas where substantial changes in the topographic surface elevation exist. Common examples of features where topographic effects could occur include ridges, canyons, steep slopes, and cliffs. The effects of topography on ground motion intensity have been observed in a number of past earthquakes beginning with the 1971 Mw 6.7, San Fernando California earthquake (Trifunac and Hudson 1971; Boore 1973), and the 1980 Mw 6.9, Irpina, Italy earthquake (Castellani et al. 1982; Sanò and Pugliese 1999). For these earthquakes, greater damage was observed in areas located on the crest or edge of topographic features compared to flat ground areas. This same higher damage concentration near topographic features was also observed in more recent earthquakes including the 1994 Mw 6.7 Northridge (Ashford and Sitar 1997), 2010 Mw 7.0 Haiti (Hough et al. 2011; Rathje et al. 2011), and 2016 Mw 6.0 Central Italy (Zimmaro and Stewart 2016) earthquakes. In addition to a significant number of earthquake records and damage observations, numerous research studies have focused on recording weak-motion seismic data using arrays of sensors deployed over topographic features (Massa et al. 2014; Barani et al. 2014; Hartzell et al. 2014; Buech et al. 2010 and many others). These studies have clearly shown the frequency-dependant amplification of seismic waves, which can occur near the crest or edge of topographic features.

Using this wealth of recorded information for comparison, it has been shown that simulations are capable of matching the amplification frequency range believed to be associated with topographic effects in a majority of cases (Assimaki and Gazetas 2004; Chávez-García et al. 1996; Le Brun et al. 1999). Furthermore, a number of analytical or empirical methods (Ashford and Sitar 1997; Paolucci 2002) have also been shown to accurately predict the observed frequency range for topographic effects (Wood and Cox 2016). However, it is still very difficult to quantify the absolute amplification/deamplification associated with topographic effects. This difficulty exists because the effect of topography on recorded ground motions is often coupled with the effect of soft soil amplification (i.e., 1D site effects). Decoupling of the two effects is often extremely difficult (Idriss and Seed 1967; Kovacs et al. 1971; May 1980; Sitar et al. 1980; Assimaki et al. 2005a, b; Assimaki and Jeong 2013). Moreover, numerical and experimental studies which attempt to quantify the amplification factor associated with topographic effects can be in substantial disagreement regarding the magnitude of the topographic effect for seismic site response. This amplification disagreement is most often observed in comparisons between ground motion records and results of numerical simulations (Bard 1982; Bard and Tucker 1985; Geli et al. 1988; Hartzell et al. 1994; Assimaki et al. 2005a, b; Assimaki and Jeong 2013). Previous experimental studies using weak motion (aftershock) data, indicate that considerable amplifications, up to ten times, have been observed using standard spectral ratio analysis, while maximum amplifications resulting from corresponding numerical models, show values nearer to 2×, using 2D models (Geli et al. 1988; Ashford et al. 1997; Athanasopoulos et al. 1999; Gazetas et al. 2002; Assimaki and Gazetas 2004; Assimaki et al. 2005a, b), and up to 4× using 3D models in different parametric analyses (Sànchez-Sesma 1985; Lee et al. 1994, Bouchon et al. 1996; Spudich 1996).

While simplification of the underlying stratigraphy and modelling simplifications have commonly been blamed for the disparity between the observed and simulated amplification results, Wood and Cox (2016) argue that the inconsistency between the choice of the reference station or reference ground motion used for the observed results and the simulated results can lead to a discrepancy between the estimated amplification values. This difference is the result of comparing numerical simulations, where the reference station is an ideal free field station, and standard spectral ratios from experimental studies, where the reference station (often located near the toe of the topographic feature) is theoretically influenced by deamplification of the ground motion at the base of a relief. In addition, the base or toe of the feature is often influenced by stratigraphic amplification because the base of the slope is frequently covered by debris-fan and/or by soft soil. Therefore, the results of most experimental studies are naturally affected by the absence of a real absolute reference, while the results of numerical models are affected by dimensional simplifications and epistemic/systematic uncertainties encountered in the simulation of real events. These difficulties are often reflected in comparison analysis making the understanding and prediction of topographic effects more difficult.

Despite differences in the estimated amplifications values, both numerical and experimental approaches have established some insights into the effects of topographic on ground motions, which are summarized below:

(i) The topographic effect phenomenon seems to be very frequency-dependent in nature with amplifications which change in amplitude according to frequency. However, the fundamental frequency of vibration occurs at wavelengths comparable to the height and/or width of the topographic feature.

(ii) Both the frequency and the amplitude response depend on the shape of relief as well as its lithology. The greatest amplification is believed to occur at the ridge crest or where the greatest convex topographic surface is located (Iwahashi and Pike 2007).

(iii) The amplitude along the short direction of the relief (perpendicular to the major elongation direction) seems to be larger than the amplitude along the long direction of the relief (Spudich 1996; Massa et al. 2010; Wood and Cox 2015).

In addition to the primary factors which influence topographic effects, other secondary factors can have an influence on the topographic effect depending on the interaction between the topographic feature and the incident seismic waves. The amplitude of the topographic effect can be modified substantially depending on the interaction between the shape and slope angles of the topographic relief and relief orientation compared to the incident seismic waves (Alfaro et al. 2012). More specifically, the parameters that influence the topographic effect are the incident angle of the wave (P, SH, SV), the slope aspect, the wavelength of the seismic wave, λ, the height/width of the feature, and the inclination, i, of the slope. It is hypothesized that other factors such as the hysteretic damping ratio, ζ, and the duration of the shaking in relation to the number of the equivalent uniform cycles, N (Bouckovalas and Papadimitriou 2003) posses a minor influence on the topographic effect. However, the latter is most relevant to slope stability assessment (Grelle et al. 2011; Grelle and Guadagno 2013). Finally, the soil-structure interaction seems to modify the location along the slope of the maximum amplification associated with topographic effects (Assimaki and Kausel 2007).

Although the amplification associated with topographic effects can be substantial, the effect is taken into account in only a few international seismic codes (European Seismic Code EC8, NTC Italian code and French Seismic Code AFPS 1995). These codes typically

modify the design response spectra using a Topographic Aggravation Factor (TAF), which is frequency-independent. The magnitude of the TAF is based on simplifying real topographic features into simple 2D relief templates that are defined based on slope inclination, i, and overall height, H of the cliff or ridge. Defining the TAF in this way, the amplification value may tend to underestimate the topographic effect for sites characterized by significant topographic features. For this reason, an approach was included in the French Seismic Code PS-92 (AFNOR 1995) to introduce a simple TAF dependent on the location of a site in respect to a step-like-slope model. Other scientific contributions on the subject, which account for the complex nature of topographic effects, have been recently proposed (Bouckovalas and Papadimitriou 2005). Specifically, Assimaki et al. (2005a, b) introduced the TAF as a function that is dependent both on the expected topographic amplification frequency and the location of the site along the relief which is used to modify the design response spectra developed using a seismic code.

2 Background

In recent years, a number of topographic amplification studies have focused on developing models and/or procedures to estimate topographic effects based on Digital Elevation Model (DEM) derived parameters. Maufroy et al. (2015) introduced topographic amplification maps that are based on the smoothed curvature parameter, defined as a wavelength dependant variable. Similarly, for seismic landslide-prone slopes, Torgoev and Havenith (2016) utilized the Arias Intensity, Ia, for a GIS-based application of Newmark's method, computing the co-seismic displacement along the topography. Among these recent methodologies, Grelle et al. (2016a) introduced a computerized model for predicting topographic amplification based on a uniform homogeneous subsurface stratigraphy, parameterized using topographic data derived from a DEM. The model is contained in the SiSeRHMap software package, which is a Python based program, which uses a hybrid model based on the metamodeling concept (Grelle et al. 2014, 2016a), to develop multi-spectral maps of seismic acceleration response and other design spectra parameters.

Metamodels, such as SiSeRHMap, are simplified models, which perform a heuristic and self-learning prediction analysis. These types of models have an extensive number of applications and provide the ability to calibrate themselves based on local experimental data. In comparison with pure physics based approaches, the predictions from metamodels can be more or less efficient depending on the ratio between the reliability of the attended metamodel results and the complexity of the problem being solved. Many of the issues and difficulties usually encountered in numerical approaches including (i) limited use by only trained researchers/technicians, (ii) inadequate and insufficient parameterization of the model in relation to complexity of the real features, and (iii) increased computational time for large datasets can be solved more simply by using a metamodeling approach. In fact, the metamodel approach has several advantages in terms of time, simplicity, and computational discount. These advantages promote the usage of the metamodels in probabilistic analysis for the reduction of epistemic and systematic uncertainties (e.g. as in Grelle et al. 2016a where SiSeRHMap was used considering a large number of the input motions along with sensitivity or/and calibration analysis which can also be easily performed on the parameterization). In addition, the reliability of modelling the 3D nature of topographic features rather than traditional 1D or 2D numerical approaches, which over simplify the results, provide a significant advantage. The above aptitude is reflected in the

ability to model large scale topographic feature on a microzontation level for strategic planning, which provides an advantage over models limited to a single topographic feature.

In this context, the present work demonstrates a clearer framework for the SiSeRHMap package and confirms the effectiveness of the package for prediction/estimation of topographic effects. Additionally, the contribution of topographic effects to the total site effect is evaluated using the seismic site response from two real cases. These cases include: (i) A study specifically design to capture topographic effects on steep hilly terrain where a dense network of seismometers were used to capture the response of the complex topography to low intensity underground mining induced seismicity and (ii) comparison analysis of topographic effects recorded from aftershock records at the crest of two ridges following the 2010, Mw 7.0, Port-au-Prince, Haiti earthquake.

3 Predictive simulation modelling

SiSeRHMap computes multispectral maps of acceleration response by coupling the effects of one-dimensional horizontal response, "the 1D stratigraphic effect" and the effects of topography, "the topographic effect". The structure of the stratigraphic-topographic model used by SiSeRHMap is referred to as a "series parallel model" (Fig. 1). The serial part of the structure considers the stratigraphic and topographic effects separately, but combines them in the frequency domain by multiplication of the 1D acceleration response spectra by the Topographic Aggravation Factor function. The parallel part of the model considers topographic effects based on two coupled factors: (i) a morphometric-dependent factor and (ii) a stiffness-dependent factor. These factors simultaneously influence the topographic effects response in terms of its frequency-dependent distribution and its spatially dependent distribution along the topography. The complex interactions between the topographic and stratigraphic effects are not expressly considered in the model, which is a limitation of the model. However, this interaction is most relevant when plastic strains are reached and given that plastic strains are often less widespread for hilly and mountain zones, due to the stiff materials often present in these areas, the interaction effects are likely more limited for hilly terrain.

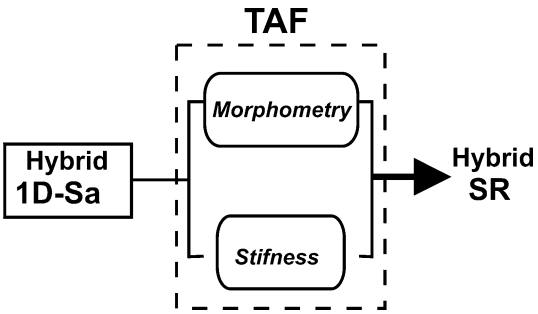

Fig. 1 Outline of stratigraphic–topographic prediction model. The model assumes the stratigraphic and topographic effects are independent effects that are combined in terms of scaling in the frequency domain the acceleration response spectra (serial connection); in turn, the topographic effect is defined by combining (parallel connection) a morphometric factor, as x, y, z-dependent of the TAF, and stiffness material factor as frequency-controller of the TAF

The metamodeling procedure for the development of the stratigraphic response maps engages most parts of the computational modules, and takes up a large part of the algorithm in SiSeRHMap. The following sections summarize the computation of the stratigraphic response, while more details are included for the topographic response since this is the main focus of the paper. However, a complete explanation of the fundamentals, mathematical/physical bases and procedures, explanation of other computational cases, and a short guide and support files are included in Grelle et al. (2016a).

3.1 Stratigraphic response

Multispectral maps of stratigraphic response are developed via a self-learning process trained on selected local 1D Vs-thickness profiles using a "GIS Cubic Model (GCM)". GCM represents the parameterized subsoil by means of an overlying structure that geometrically reproduces a pseudo-3D subsoil model, which is composed of a flat-spatial distribution of one-dimensional Vs-thickness profiles. In the GCM, an assigned number of 1D Vs-thickness profiles are selected, by Montecarlo technique, and the response spectra is computed using the equivalent linear approach. These response spectra become the targets for training in the self-learning process. After the training processes, maps can be produced which describe the 1D response over the entire map area by resolving the trained model in GCM. Significant additional information on the models and calibration procedures are available in Grelle et al. (2016a).

3.2 Topographic Aggravation Factor (TAF)

Multispectral maps of Topographic Aggravation Factor (TAF) are computed as a non-linear function in the frequency domain for scaling the 1D seismic response. In this way, the TAF is identify as the spectral ratio between the response on the topographic surface and a damped 1D free-field response (e.g. as defined in Assimaki and Gazetas 2004; Assimaki et al. 2005a, b; Assimaki and Kausel 2007). The "gray-box model", as defined by Grelle et al. (2016b), is used to estimate the TAF using DEM derived input data. The topographic prediction model is based on the results of Geli's dimensionless law of 2D uniform relief (Geli et al. 1988) and on the step-slope model by Ashford et al. (1997). The model was optimized using a comparison analysis with the results of 3D numerical computations of the frequency-dependent amplification factor in the Albino Plateau area (France) reported in Maufroy et al. (2012). The results were also shown to be in agreement with spectral ratio analysis from weak ground motion data-sets on Narni prominent hill (Italy) (Barani et al. 2014). This current work is an additional step in the validation of the model. A brief discussion of the characteristics and fundamental bases of the model are provided below. However, a more detailed discussion regarding the model can be found in Grelle et al. (2016a).

As discussed previously, the topographic model consists of two parallel inter-dependant factors: (i) morphometric-dependent factor and (ii) stiffness-dependent factor. These factors simultaneously influence the TAF in terms of its frequency-dependent distribution and its spatially-dependent distribution along the reliefs. The computations for each of these factors is discussed in more detail below.

Morphometric-dependent factor: The preliminary morphometric raster-maps are developed using typical GIS-platform tools to compute: (i) a digital elevation model, DEM; (ii) slope angle, i (the arctangent of the first derivate of the DEM), and (iii) curvature, c (the second derivative of the DEM). The curvature assumes a preeminent role in

the topographic model, because areas of high curvature are related to areas of high amplification. Additional morphometric raster-maps are computed based on these maps and include the local slope height, H, and the relief height, H_R, both computed in relation to the basal surface of the relief (BSR) where H is assumed to be zero meters. BSR is an irregular surface determined through a scanning process, which combines 2D profiles along the North–South and East–West direction (Appendix C in Grelle et al. 2016a). The BSR is developed through a virtual association of local idealized Geli's half-hills with real topographic features. A relief ratio map, $r_H = H/H_R$ is then calculated from the BSR, which is a relative slope position index with values between 0 (toe), and 1 (ridge crest).

Stiffness-dependent factor: To estimate the velocity of the reliefs, the material is considered homogeneous. However, to account for the possible vertical variation (increase) in stiffness or possible layering of the relief, an equivalent value of the shear wave velocity is estimated for the relief. The equivalent shear wave velocity approximates the behaviour of the natural relief in terms of the TAF, which is function of the geometry and global velocity of the feature. The inclusion of near surface soft layers (soft soils) in the estimation of the equivalent shear wave velocity has a low influence for larger features. However, the influence is more important for smaller features. In either case, the contribution of near surface soft materials is included in the equivalent velocity computation.

The proposed model is based on the DEM variables mentioned above that provide a substantial parametric structure able to reproduce the idealized geometric form of a half Geli's relief. These variables are considered in relation to their physical influence on the topographic amplification effect. In terms of curvature, a positive value represents convex features such as ridges or edges, while a negative value represents concave features, such as a valley. The curvature of a typical topographic feature is greatest near the ridge, where the slope angle is small and near to zero, and near zero along the relief, where the slope angle is constant. Near the valley floor, the slope angle decreases and the curvature is negative. The maximum curvature considered by the model is at the minimum curvature radius of the 3D surface (largest change in slope angle). This condition implies that the topographic amplification model tends to predict the maximum amplification for a motion polarized transverse to the relief (i.e., in a direction perpendicular to the elongation of the relief).

In numerical terms, the SiSeRHMap topographic model (Fig. 2) was created to determine the location of positive amplification, therefore the model returns TAFs equal to 1 where topographic features related to deamplification are present (i.e., valleys and regular slope toes). The model is characterized by a non-linear law with a spectral peak at a dimensionless frequency equal to the topographic fundamental frequency defined as $H/\lambda = 0.2$ (Ashford and Sitar 2002) and a secondary model function in order to envelop the other components contributing to topographic amplification at higher frequencies. These secondary model functions include higher modes of the relief vibration (e.g., an idealised shear-beam in Cauzzi et al. 2011 and Paolucci 2002), but mainly include the superposition effects of reflected waves coming off boundaries of the soil layers, diffracted waves due to the topographic irregularity, and Rayleigh waves generate by transmitted and reflected waves incidence with the slope surface (Assimaki and Gazetas 2004). These waves propagate along the surface converging at the crest or projections of the topographic surface (Ohtsuki and Harumi 1983; Jafarzadeh et al. 2015).

Overall, the GIS-hybrid model at the base of SiSeRHMap is unique in the prediction of surface seismic response for complex topographic features coupling the stratigraphic-topographic effect as a serial-parallel problem. However, its computational bases can be associate with other models or procedures that try to predict the topographic amplification

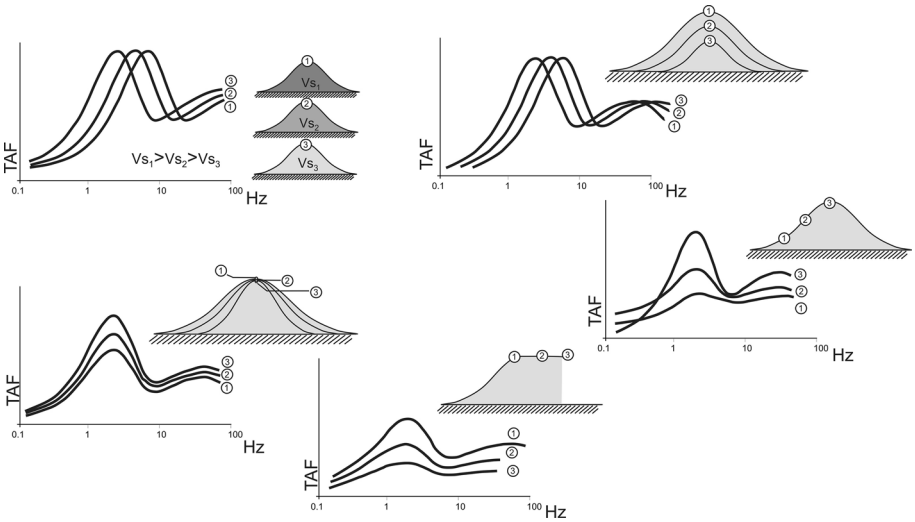

Fig. 2 Some general shapes of the topographic model assumed by considering different location on 2D reliefs and different morphometry details. In the DEM computation, the shape of the curve can substantially change in relationship to the 3D morphological complexity of the reliefs

factor using parameters derived from GIS map data and optimized empirical/heuristic models. For example, Maufroy et al. (2015) introduced the FSC-proxy based on the smoothed curvature function for estimating the topographic amplification factor. The function was calibrated by the results of a 3D numerical model applied to a natural landscape in France, which was modelled as a uniform material. In this model, the topographic amplification factor is defined based on the MRM analysis. Also as an example, Rai et al. (2016) propose an empirical prediction approach, at the same time SiSeRHMap was being introduced, based on a regression analysis of results obtained using 2D numerical models applied in a multi-directional way. The calibration used a natural regular slope (equilateral along the transversal direction) composed of a uniform material. In this approach, the topographic amplification factor was estimated in reference to the 1D numerical response of uniform flat ground. However, a procedure for GIS spatial distribution of the results was not discussed. In addition, the accuracy of each approach at predicting the topographic response for areas outside their calibration datasets has not been performed.

4 Application case histories

4.1 East Mountain area (Utah, USA)

4.1.1 East Mountain background information

A topographic effects study was conducted in the East Mountain area of the Manti-La Sal National Forest, located in central-eastern Utah, USA. The area is characterized by steep complex topography, which lies within the Wasatch Plateau region approximately 95 km southeast of Provo, Utah. The area sits over 3000 m above mean sea level at its highest

point with approximately 1000 m of relief from ridge to valley floor. The geology of the area is characterized by sedimentary formations of sandstone and shale (Arabasz and Julander 1986; Williams and Arabasz 1989). Seismicity in the area is a combination of natural and induced seismicity with the majority of the seismic events tied to underground long wall coal mining in the area (Wong 1993). This induced seismicity is a low-intensity form of frequent and predictable seismicity generated not by mine blasts, but by implosions and/or stress redistribution in the subsurface. The seismic energy is dominated by compensated linear-vector diploes or double couple shear source mechanisms (Wong 1993).

To record the seismicity in the area, an array of 22 broadband stations were deployed over the terrain in an H pattern forming two parallel lines (A and B) and one short

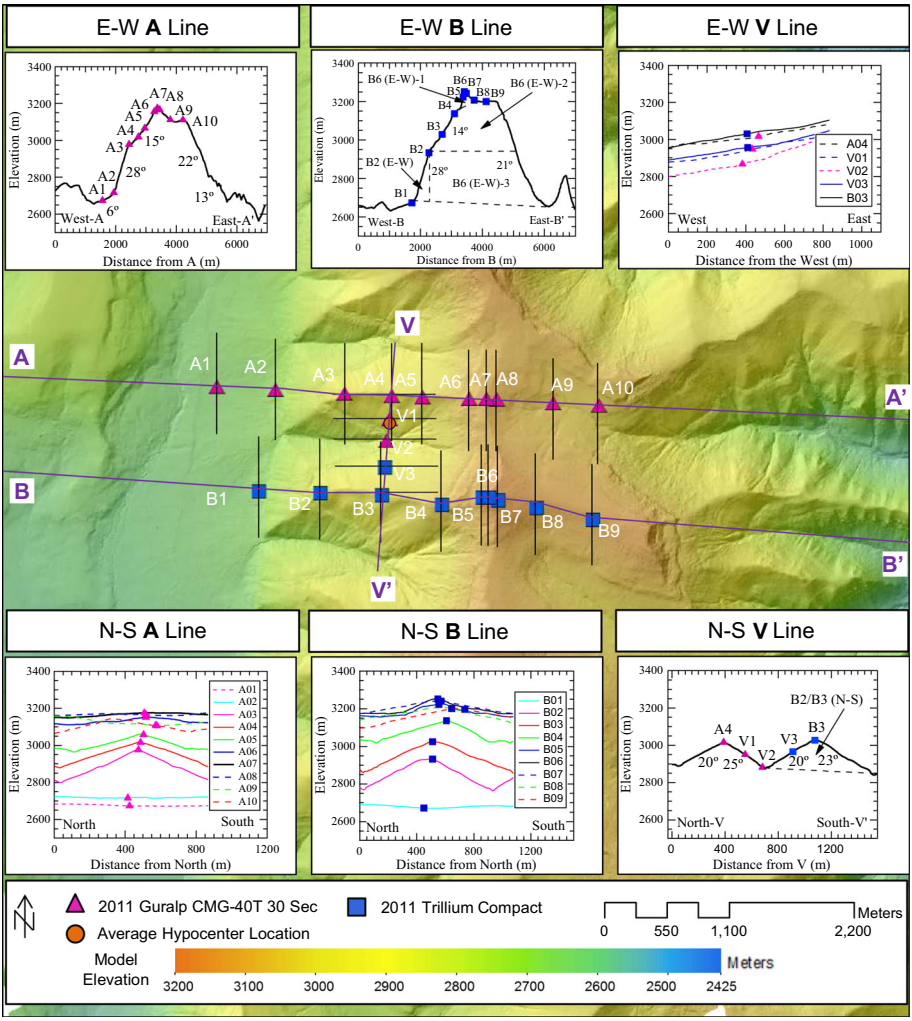

Fig. 3 Digital elevation model of East Mountain study area with seismic station locations used during recording (N–S and E–W cross sectional profiles of the features shown for profiles A–A′, B–B′, V–V′ and additional sub cross sections. Sub cross sections denoted as black lines crossing through each sensor). The average hypocenter for the study is shown within the main topographic array

perpendicular line (V) as shown in Fig. 3. The A and B lines start in the western valley and continue up the crest of separate, but parallel east–west trending sub-ridges that buttress the main north–south trending ridge. The V line instruments a small valley that sits between the two east–west trending sub-ridges, which are instrumented by lines A and B. The shear wave velocity (Vs) profile of the area was estimated using the Multi-Channel Analysis of Surface Waves (MASW) method. Testing was conducted near Station B7. The results indicate the site is underlined by a thin soil layer approximately 7.6 m thick with a Vs of 300 m/s underlined by a weather rock with a thickness of approximately 19.8 m with a Vs of 790 m/s and finally a hard rock layer with thickness of at least 39.6 m with a Vs of 1400 m/s. Since the Vs profile did not extend to the full depth of the relief an additional layer was added to the model with a Vs of 2040 m/s, which is based on other velocity models in the area (Pechmann et al. 2008). Further details regarding the experimental setup can be found in Wood and Cox (2015).

The seismic activity in the area was monitored using the array of stations for a total of 10 days, which resulted in 52 weak motion events recorded by the array. These events had local magnitudes (M_L) less than 1.6 as calculated by the University of Utah Seismograph Station network. Peak ground velocities (PGV) at Station B6 varied from 0.0071 to 0.1379 mm/s. The hypocenter location of each event was determined using Hypoellipse (Klein 1978) and an adjusted velocity model from previous studies in the area (Arabasz et al. 2002; Pechmann et al. 2008). The hypocenter locations were used to correct for geometric spreading in the data due to the close proximity of the source compared to the size of the array (see Fig. 3). The events were processed as detailed in Wood and Cox (2015) and used to evaluate the most common methods used to processes experimental topographic effects data. It was determined by Wood and Cox (2016) through comparisons of the Standard Spectral Ratio (SSR) and the Median Reference Method (MRM) (Maufroy et al. 2012), that the MRM resulted in the most consistent spectral estimates and most accurate and consistent amplification estimates for the recorded events. However, the East Mountain study has a number of attributes which make it a theoretically optimum location and dataset for understanding the effects of topography on ground motions. These features include a large dataset of recorded ground motions and instrumented topographic features, which are geometrically advantageous. These topographic features include the east–west trending subridges instrumented by lines A and B, which have the following features: (i) a regular (equilateral) two dimensional shape along the transversal axis (east–west direction), (ii) ridges that are similar in shape with an equal width, (iii) an equal cross-sectional width for much of length of each ridge, (iv) a relative thin layer of soil and weather bedrock, which isolates the potential 1D site effects to the higher frequency range, (v) relative high reliefs compared to most studies. The thin layers of soil and weather rock significantly increase the potential to separate the influence of 1D site effects from topographic effects. In particular, the transfer function calculated for the site indicates 1D site effects are most likely to occur at frequencies greater than 5 Hz, which is higher than the expected topographic effects frequency range for the site (Wood and Cox 2016). Therefore, this case is used to evaluate the reliability of SiSeRHMap in terms of the 3D topographic effect. The map of stratigraphic response was not computed because of the limited amount of subsurface data available over the study area.

4.1.2 East Mountain results

Multi-spectral maps of Topographic Aggravation Factor (TAF) (shown in Fig. 4) were computed for vibration frequencies of 10, 5, 4, 3, 2, 1, 0.9, 0.8, 0.7, 0.6, 0.5, 0.4, and

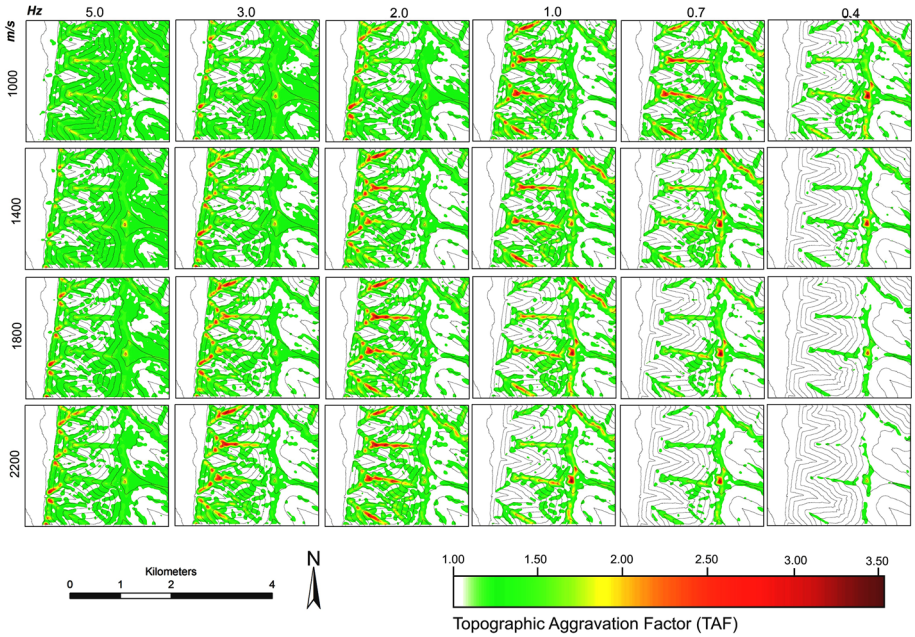

Fig. 4 Twenty-four maps of TAF for the East Mountain area. Computed using SiSeRHMap for the four equivalent uniform Vs profiles (1000, 1400, 1800, and 2200 m/s) and for frequencies of 5, 3, 2, 1, 0.7, and 0.4 Hz

0.2 Hz, assuming different equivalent uniform shear wave velocities of 1000, 1400, 1800 and 2200 m/s. The final two equivalent uniform Vs values are based on Vs-profiles collected using MASW near the crest of Line B by Wood and Cox (2016) and consistent with the time-averaged Vs used by Wood and Cox (2016) to estimate the topographic fundamental frequency for the features. Examining the distribution of TAFs across the instrumented area, the highest spectral values of TAFs are not exclusively found along the major N–S trending ridge, but are frequently associated to the E–W trending sub-ridges buttressing the main ridge and primarily at the western edge of the peninsula type features at the end of the sub-ridges. The maximum estimated TAF of 3.61 at 1.00 Hz is located at the edge of the peninsula near Station A3 (TAF = 3.42) and was estimated using a Vs_{eq} equal to 1000 m/s. However, values of TAF around 3.0 are also observed for the crest of the main N–S trending ridge at the location of the highest relief at 439 m. In general, the multispectral maps highlight high amplifications along sharp ridges that quickly decrease along the lateral slopes (down slope from the ridge), this is in agreement with experimental spectral ratios recorded along Line V in the experiment.

Figure 5 shows a comparison of spectral ratios estimated using the average SSR and MRM results from recorded events during the East Mountain Study and TAFs extracted from the multi-spectral maps developed using SiSeRHMap. For the SSR and MRM results, the resultant vector (root sum squared) of the N–S and E–W horizontal components is shown. For stations in Line A, the fundamental topographic frequency range, identified using the SSR and MRM results, is 0.2–1.0 Hz with the peak spectral ratio at 0.5–0.6 Hz, which matches reasonably well with the results from the SiSeRHMap at many of the stations. For stations in Line B, the fundamental topographic frequency range, identified

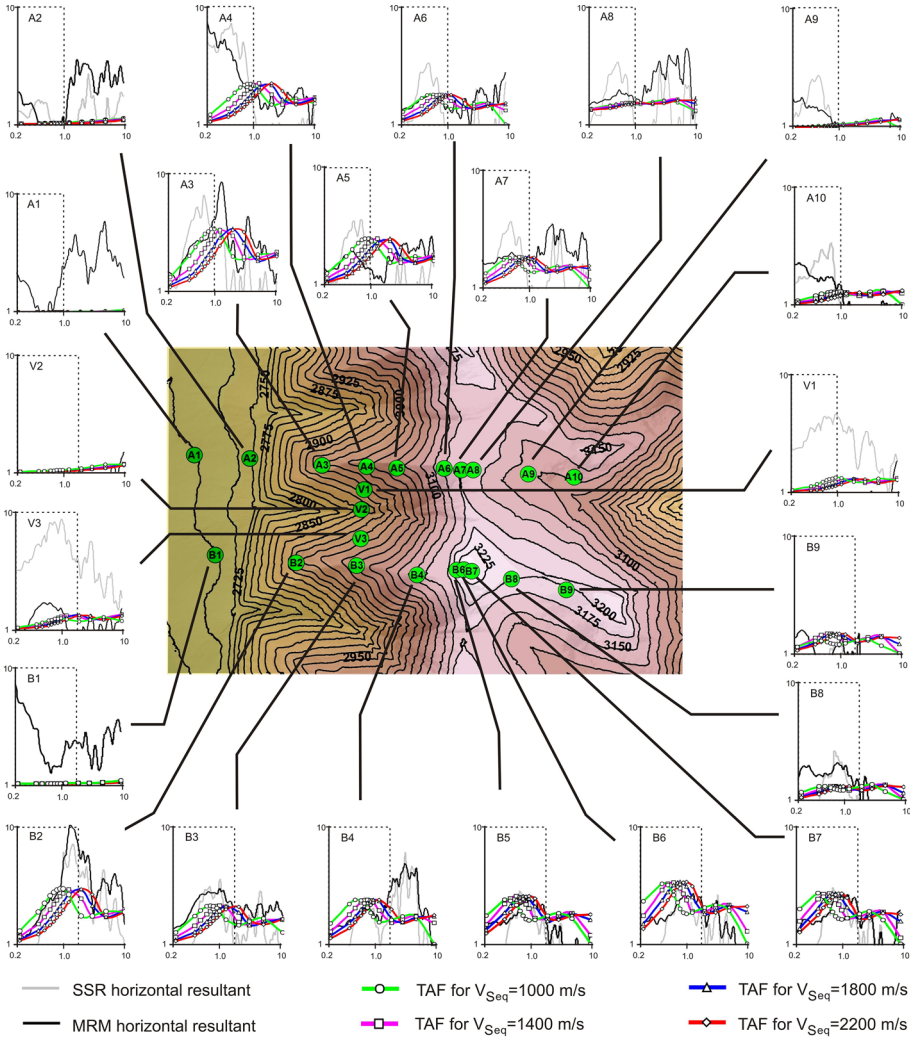

Fig. 5 Local frequency distribution of TAF values extracts from multispectral map set and MRM and SSR spectral ratios for stations in Line A, Line B and Line V. The dashed line box encompasses the estimated topographic fundamental frequency vibration range

using the SSR and MRM results, is at a slightly higher and wider frequency range from 0.2 to 2.0 Hz with the peak spectral ratio at 0.7–1.0 Hz. For both lines, the maximum amplification, estimated using SSR and MRM, was calculated for the crest of the peninsula like features at the western edge of Lines A and B (Stations A3, A4, B2, and B3). However, significant amplifications were also calculated along the main N–S trending ridge for Stations A6, A7, A8, B5, B6, and B7. Comparing the TAF determined using the four different equivalent uniform Vs values for the features (i.e., 1000, 1400, 1800, and 2200 m/s), the results from the lower velocity ranges (1000–1400 m/s) tend to perform the best for Line A. However, for Line B the medium velocity ranges (1400–1800 m/s) tend to perform the best.

To further compare the experimental results and TAF determined using SiSeRHMap, the average spectral ratio from the SSR and MRM and average TAF for the best fitting average velocity values for each feature are shown in Fig. 6 for the expected topographic amplification frequency range for each line (6c and 6d) and a higher frequency range (6e and 6f). These results confirm the relatively good match between the experimental and SiSeRHMap results in the estimated topographic frequency range, but also in the higher frequency range. Overall, the TAF seems to have a tendency to under-predict slightly (though there are a number of over-predictions) in the fundamental frequency range, which is often the case when comparing experimental and numerical results for topographic effects studies. In particular, the average percent difference between the MRM and the TAF for the estimated topographic fundamental frequency range (FFR) and high frequency range (HFR) are − 12 and 28%, respectively for Line A assuming an equivalent Vs of 1000 m/s and excluding Station A1 (the relief toe station). For Line B, assuming an equivalent Vs of 1400 m/s, the average percent differences are − 23 and 1.5%, respectively. On the other hand, the average percent difference between the SSR and the average TAF values in the above frequency ranges are − 30 and − 54% for the FFR and HFR, respectively for Line A. For Line B, assuming an equivalent Vs of 1400 m/s, the average percent differences are 8 and 62% for the FFR and HRF, respectively. This indicates the SiSeRHMap results match better with the MRM, which again was determined to be more consistent and accurate method for estimating topographic effects by Wood and Cox (2016).

Examining Fig. 6c–f more closely, several specific observations are discussed below. For the peninsula like features instrumented by Stations A3/A4 and B2/B3, an excellent fit (∼ 5% difference) is observed at Station A3 (most protruding section of the feature)

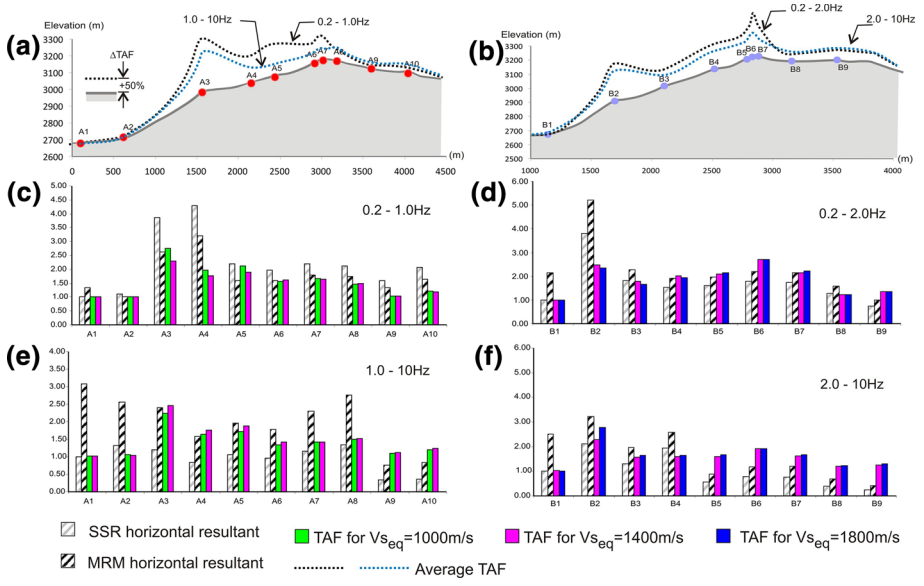

Fig. 6 Comparison between predicted TAF values and experimental spectral ratio in terms of spectral average values that are calculated in the topographic fundamental topographic frequency range (dashed line box in Fig. 5) and higher frequency range; **a** topographic profile for Line A and **b** topographic profile for Line B. Distribution of average TAFs for each station: **c** low frequency Line A, **d** low frequency Line B, **e** high frequency Line A, and **f** high frequency Line B

between the TAF and MRM results for both the fundamental and high frequency range. However, a much poorer fit is observed at a similar location in the B line (B2) with the TAF significantly underestimating the MRM results by approximately 200% in the fundamental topographic frequency range. In addition, poor fits are also observed for Stations A4 and B3 with the TAF underestimating the MRM experimental results by 65 and 30%, respectively. While these differences are significant, it is also observed that there is equally poor agreement between the SSR and MRM results for these locations. Moreover, the coefficient of variation of the spectral ratios calculated for these Stations using the 52 recorded events was approximately twice as high as Stations A7 and B6 located at the crest of the major N–S trending ridge (Wood 2013). This further indicates the amplifications in this area (and possibly for this type of feature in general) are more variable than those for simple 2D ridge features.

Comparing the results from the crest of the main N–S trending ridge (Stations A6, A7, A8, B5, B6, and B7), a substantial overestimation of 30% is observed for the TAF compared to the MRM results in fundamental frequency range for Station B6; however, good to excellent agreement (0–10% difference) is observed at the other station locations near the crest in the fundamental topographic frequency range.

By analysing the peaks in the fundamental topographic frequency ranges for each station, it is possible to understand the reliability of the computational topographic model

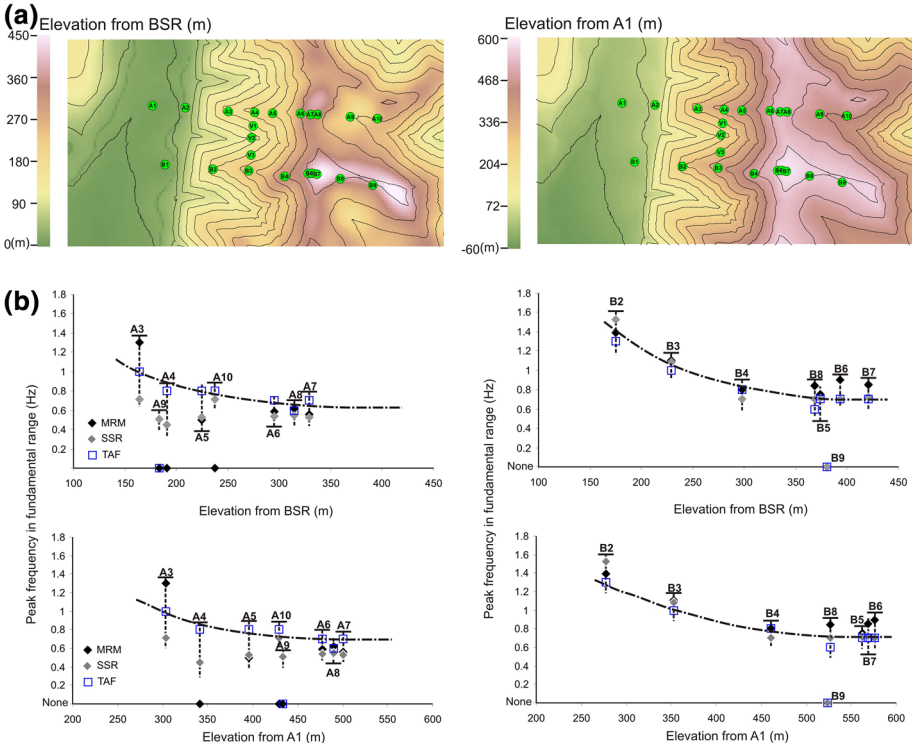

Fig. 7 Peak frequency in fundamental frequency range for stations in Line A and Line B in relation to elevation computed both from BSR and Station A1 elevation: **a** DEM from BSR altitude (left) DEM from A1 station altitude (right); **b** experimental spectral ratio and TAF values distribution the black dashed lines represent the frequency migration of TAFs in relation to the top relief elevation

at the base of SiSeRHMap (Fig. 7). Specifically, considering the consistent width of the E–W trending sub-ridge features, it seems that the frequency migration, along Lines A and B in the intervals A3–A5 and B2–B4, is more in agreement with the increased elevation along the ridge rather than the similar widths of the ridge under each station (see Fig. 3). As shown in Fig. 7, the peak fundamental frequency for these stations decreases (see black dashed lines) as one moves from the lower stations (A3 and B2) to the upper stations (A5 and B4) (shown as a function of the elevation of Station A1 and the Basal Surface Relief). This behaviour is more apparent for Line B, but is still observed to a lesser extent in Line A. For the sub-ridge zone, polarization analysis of Line B stations, conducted by Wood and Cox (2016), confirms amplification in the transversal direction to the sub-ridge (N–S direction) for both the MMR and SSR methods. However, Stations B6–B8 located on the main N–S trending ridge, which have an E–W amplification directionality, have very similar fundamental amplification frequencies to Station B4. However, the width of sub-ridge under Station B4 is significantly less (about 3 times) than the width of the main ridge under Stations B6–B8. This indicates that the fundamental topographic frequency for a feature may be more related to the height/elevation of a feature rather than the width of the feature or that larger features need to broken up into smaller features where changes in slope occur similar to how Wood and Cox (2016) broke up the main ridge into smaller ridges to compute the fundamental topographic frequency (see Fig. 3).

4.2 Port-au-Prince area (Haiti)

4.2.1 Port-au-Prince Background Information

In this section, a simulation was performed in an area with a well-documented observation of topographic effects related to the 2010, Mw 7.0, Port-au-Prince, Haiti earthquake. A number of aftershocks were recorded by the United States Geological Survey using portable seismographic stations (Hough et al. 2010), installed after the main shock, in different characteristic locations across the city of Port-au-Prince. A notable discrepancy in the ground motion response was recognized at two of these seismic stations (HHMT and HCEA, shown in Fig. 8), which are located at the top of two neighbouring hills (Hough et al. 2010). The two topographic features have substantially different shapes (Fig. 9). The HHMT station is located on an isolate feature with an elongation along one axis with a

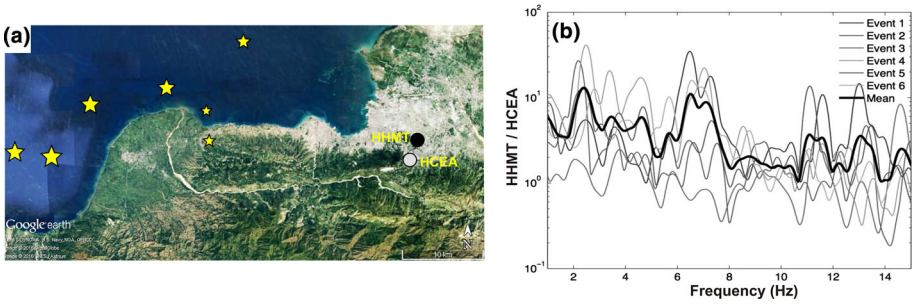

Fig. 8 Aftershock from the 2010 Haiti earthquake recorded at the HHMT and HCEA seismic stations: **a** satellite map of the source area (stars cluster: big star are the moderate events, small stars are the weaker events) and the location of the stations (from Hough et al. 2010); **b** ground motion ratio for the two stations (from Assimaki and Jeong 2013)

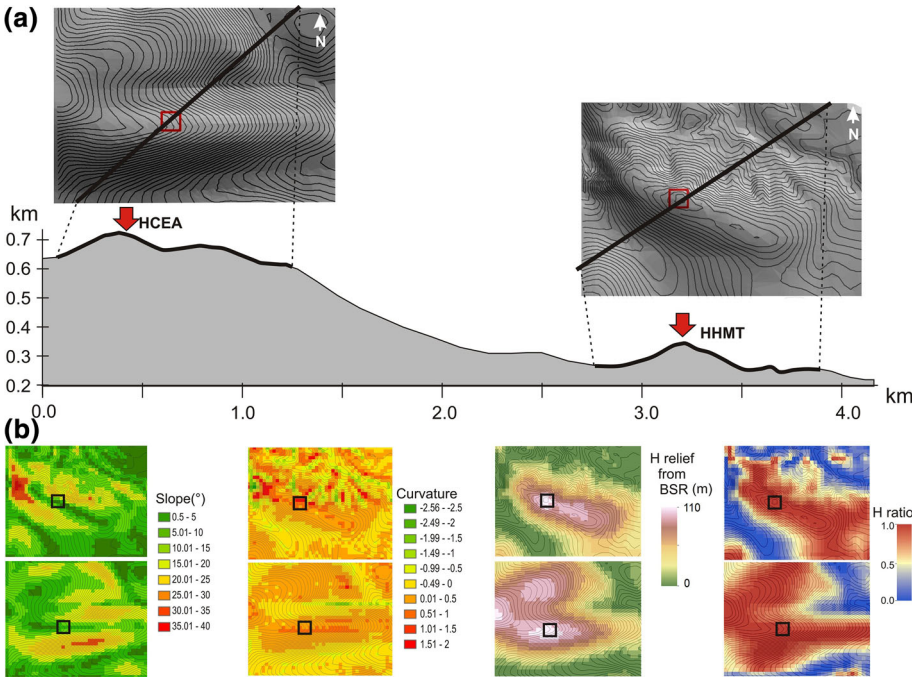

Fig. 9 Topographic features related to the HHMT and HCEA seismic station places: **a** elevation profile; **b** DEM with horizontal resolution of 30 m, the box represents the station locations

width and length at the base of about 800 m and 1600 m, respectively. The HCEA station is located on a more complex feature, which is a sub-ridge to a larger main ridge. Despite the difference between the ridges, it is possible to identify a similar 2D cross sectional shape as was done by Assimaki and Jeong (2013) for their 2D numerical analysis. These 2D cross sections are shown in Fig. 9a. Despite the hills being located only a few kilometres apart and having the same orientation in relation to the seismic sources, the HHMT station consistently recorded a larger ground motion amplitude for aftershocks and more severe structural damage (e.g., collapses) was observed at the nearby Hotel Montana, in the district of Pétionville (Hough et al. 2010). The cause of the higher amplitude and increase damaged at HHMT compared to HCEA was identified as topographic effects by Hough et al. (2010, 2011).

To better understand the role of topographic effects on the recorded ground motions, a comparison analysis based on the HHMT and HCEA record-sets was conducted by Assimaki and Jeong (2013). The authors utilized six ground-motion aftershocks with magnitudes between 3.6 and 4.4, which were located in an area approximately 40 km from the seismic stations (Fig. 8a). Shear wave velocity (Vs) profiles were measured at the seismic stations using the multichannel analysis of the surface waves (MASW) to a depth of 30 m (Cox et al. 2011). From these Vs profiles, the HHMT site has a Vs30 = 626 m/s, which is much lower than the Vs30 of the HCEA site at 1024 m/s. Moreover, the HCEA site is characterized by pelagic limestone with stiffness increasing with depth, while the HHMT consists of marine fan deposit underlined by weak marls/limestone. Based on the geological setting of the metropolitan area of Port-au-Prince (Cox et al. 2011; Terrier et al. 2014), this weak marls/limestone is underlined by a stiff limestone layer at depth. Assimaki

and Jeong (2013) hypothesize that this additional stiffened layer constituting the local bedrock is present at approximately 100 m below the surface at the HHMT site. Based on the low intensity of the recorded aftershocks in addition to the minor 1D site effects (very thin soil layer at the surface), Assimaki and Jeong (2013) and Fleur et al. (2016) used the HCEA as a reference station for estimating the amplification factors for other recording stations.

From the spectral ratio distribution of the six aftershock records shown in Fig. 8b, it can be noted that widely scattered amplification occurs over much of the considered frequency range (1–15 Hz) with the exception of the frequency range from 8 to 11 Hz and subordinately around 5.5 Hz, where the scattering appears smallest. Peaks in the spectral ratio are observed between 6.5 and 8.0 Hz and at approximately 3 Hz, all with comparable amplitude. The scatter in the spectral ratios for the five aftershock records can be attributed to the source azimuth and the interaction with the underground geological structure and/or three-dimensional relief surface (Paolucci et al. 1999; Maufroy et al. 2012).

4.2.2 Port-au-Prince results

In contrast to the comparison analysis for the East Mountain Area, the SiSeRHMap model was used in its stratigraphic and topographic coupling mode for the Port-au-Price study as illustrated in Fig. 2. Since the ground motion records are only available at the HHMT and HCEA stations (positioned at the crest of each feature), the 1D-stratigraphic acceleration response spectra was only computed for the two station locations using the Vs profiles available at each station. Since the SiSeRHMap model was used in an atypical way (i.e., computations at single discrete points), it prevents the running of the computational modules that develop stratigraphic response maps, such as the *metamodel training* and the stratigraphic multispectral *map generator*. These portions of the model were not run because it was not possible to build the layered subsoil models without additional data. Additionally, these maps were not needed to achieve the goals of this study. Although the stratigraphic response maps were not computed, the TAF maps were computed and their values are the focus of this section. In summary, the seismic response was determined by combining the 1D spectral acceleration response computed at the two stations locations and frequency-scaled by discrete TAF values extracted from the spectral map set computed using the 3D surface topographic module of the code.

To compare the response of the two stations, the input motion used was the recorded ground motion from the horizontal north–south corrected (baseline and trend) acceleration of the main shock of the Haiti earthquake recorded by the SDDR station on 2010/01/12 at 21:53 (USGS source) with a PGA of 0.107 g and epicentral distance of 143.6 km located in Presa de Sabenta—Dominican Republic (From USGS: http://ngawest2.berkeley.edu/). The subsurface conditions at the site are classified as rock. This motion has been used as a reference waveform in several previous studies on regional seismicity (Özel et al. 2011; Hancilar et al. 2014).

For the 1D site effects analysis, the Vs profile reported by Cox et al. (2011) was directly used in the analysis for the HCEA site. However, a parametric analysis using five Vs profiles derived from the Cox et al. (2011) were used for the HHMT site (see Fig. 10). The parametric analysis was necessary at the HHMT (Fig. 10a) because hard bedrock (Vs $>$ 2000 m/s) similar to the HCEA site was not encountered at the HHMT. The five models included Model A, which extended the final layer from the profile (Vs $=$ 1230 m/s) to the full depth of the model (i.e., bedrock velocity 1230 m/s), and models B, C, D, and E, which have different depths to an assumed bedrock velocity of 2300 m/s (the same

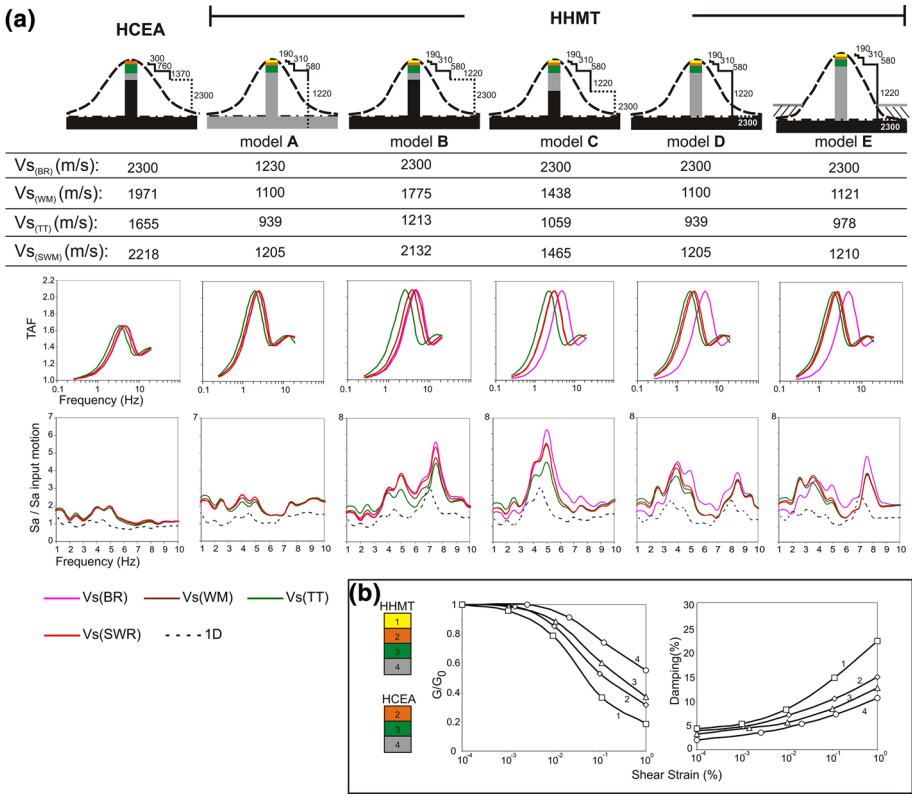

Fig. 10 Seismic response computed by serial-parallel model of SiSeRHMap for HCEA model and for different hypothesized Vs-depth HHMT models: **a** models and relative spectral ratio results arranged vertically; **b** dynamic degradation curves of the material constituting the Vs-depth models

bedrock velocity observed at the HCEA site). Therefore, the thickness of the soft rock layer (1230 m/s) for each model is 20, 50, 80, and 100 m resulting in a bedrock depth for each model of 36, 66, 96 and 106 m, respectively. For Model E, the height of the topographic feature was increased by 20 m to account for the existence of a soft soil layer at the base of the ridge which may obscure the true height and width of the feature. The 1D site effects analysis was conducted using an equivalent linear analysis (Appendix A in Grelle et al. 2016a) and output motions were obtained at a depth of 0.50 m. The modulus reduction and damping curves were chosen for similar general material from an unpublished Italian dataset based on the stiffness and type of the materials (Fig. 10b). Based on the analyses, the strain levels encountered were primarily in the linear strain range. Therefore, the low shear strain levels permit an adequate comparison of the amplification ratio between HHMT and HCEA stations for the measured aftershock motions.

For the topographic effects estimates, the TAFs for the two stations locations were determined by averaging the mapped TAF values over a square area 90 m by 90 m centered on each station location. For these areas, the average surface curvature values are greater at the HHMT station (0.87) than at the HCEA station (0.41) (see Fig. 9b). The equivalent shear wave velocity, Vs_{eq} for each feature was assumed to be a uniform value

that represents the global velocity of the feature for the TAF calculations. This Vs_{eq} value was defined using one of four different shear wave velocity-thickness relationships (Equations from 1 to 4). These relationships are based on either the bedrock velocity ($V_{S(BR)}$, Eq. 1), the weighted arithmetic mean ($V_{S(WM)}$, Eq. 2), the time-averaged shear wave velocity ($V_{S(TT)}$, Eq. 3), or the weighted harmonic mean shear wave velocity ($V_{S(SWN)}$, Eq. 4). Equations 2–4 are based on the materials located above the bedrock layer and are applied to each of the Vs models (A-E) mentioned previously. Overall, the $V_{S(BR)}$ equation provides the highest stiffness for the each of Vs models (A-E) followed by the $V_{S(SWM)}$ equation and the $V_{S(WM)}$ equation, while the $V_{S(TT)}$ equation provides the lowest stiffness for each of the Vs models.

$$Vs_{(BR)} = Vs_n \tag{1}$$

$$Vs_{(WM)} = \frac{\sum_{i=1}^{n} Vs_i h_i}{\sum_{i=1}^{n} h_i} \tag{2}$$

$$Vs_{(TT)} = \frac{\sum_{i=1}^{n} h_i}{\sum_{i=1}^{n} \frac{h_i}{Vs_i}} \tag{3}$$

$$Vs_{(SWM)} = \frac{\sum_{i=1}^{n} Vs_i h_i^2}{\sum_{i=1}^{n} h_i^2} \tag{4}$$

In Fig. 10, the spectral TAF values and acceleration response spectra (output/input) for the HHMT and HCEA sites are compared for the various Vs models used for the parametric study. Overall, TAF values for the HHMT site are substantially higher than for the HCEA site for all the parametric models and Vs_{eq} equations. Specifically, the HHMT site has a peak TAF of 2.1 for each Vs_{eq} and Vs model used in the study, while the HCEA site has a peak TAF of 1.65. This difference is attributed to a lower surface curvature value at the HCEA site. The amplification peaks for the two sites also occur at slightly different frequencies with the HCEA site having amplification peaks between 3.5 and 5 Hz and the HHMT site having amplification peaks between 2 and 6 Hz. For the HHMT site, the peak amplification frequency is significantly more variable than for the HCEA site mostly due to the significant differences in the assumed Vs_{eq} values used for each model. In general, the lowest peak amplification frequencies at the HHMT site are observed when using the $V_{S(TT)}$ equation along with velocity models A, D and E, while the highest frequencies are observed when using the $V_{S(BR)}$ equation with velocity models B and C.

The acceleration response spectra in Fig. 10 for the coupled stratigraphic-topographic SiSeRHMap model were computed using a damping ratio of $\zeta = 1\%$. These spectra are compared to the acceleration response spectra calculated using an un-damped single degree of freedom (SDOF) system with Vs profiles shown in Fig. 10a. The acceleration response spectra are normalized by the input motion (SDDR record) to generate the spectral ratios shown in Fig. 10. The most significant amplification is observed for the HHMT parametric models with an additional assumed stiff bedrock layer in the subsurface (i.e., models B, C, D, and E). An amplification over five times is observed for these models. In contrast, much smaller amplifications (< 2) are observed for the HCEA site and HHMT model A. The

large amplification for the HHMT site (models B-E) tend to occur at a low frequency range (2–5 Hz) and also at a higher frequency range (7–8.5 Hz), but both are related to the depth to bedrock and equivalent stiffness of each model.

By using the same input motion in the computation of the seismic response at the HHMT and HCEA sites, their spectral ratios can be compared with the SSR (HHMT/HCEA) from the recorded aftershock records (obtained from Assimaki and Jeong 2013). However, because of the simplified process the model is based on (Fig. 1), the spectral response cannot be directly used in a comparison analysis. Therefore, a deconvolution algorithm-based process is used to develop the transfer functions at both sites. In the deconvolution, the Transfer Function, TF, was defined by a reverse spectral function obtained from a process similar to that introduced by Fahjan and Özdemir (2008). This process consists of the iterative modification of the Fourier spectral amplitude via a 2D array with size equal to the number of iterations (rows) and length of the spectral elements (columns). In this way, each row element of the array is calculated using a progressive approximation ratio, and therefore the final transfer function is given by a row product of the coefficient array obtained from the iteration. Therefore, in a generic ith loop, this ratio is between the spectral response target and the current ith spectral response. The ith coefficient array is used for spectral scaling in the ith + 1 iteration. In this specific case, the target response spectra are the SiSeRHMap response spectra computed for the HHMT and HCEA sites. The algorithm is run by a dedicated code, which is used to modify the natural accelerograms, the SDDR's accelerogram in this specific case, in order to match them to the assigned spectrum target. This code will be the subject of a future paper.

Assuming that the same input motion occurred at the base of the HHMT and HCEA sites, the mean of the standard spectral ratios of the aftershock records can be used for comparison with the results from SiSeRHMap. In this way, the theoretical transfer function for both stations, obtained using the SDDR input motion, are determined independently of each station, and then used to estimate the spectral ratio between the stations. The transfer functions obtained in this way are defined in terms of absolute amplification (Fig. 9). However, the estimated transfer function ratio between the two stations, which are compared to the recorded standard spectral ratio values (HHMT/HCEA), constitute the relative amplitude comparison in Fig. 10. In regards to Fleur et al. (2016), the HCEA station was used as a reference site in an SSR analysis because relative low amplitudes were measured during the aftershock events. However, a non-flat average value of horizontal to vertical spectral ratio (H/V analysis) was observed at the HCEA site. This non-flat response highlights the difficulty in considering HCEA totally free of seismic amplification (Fleur et al. 2016). That said, the HCEA site is still used as a reference site in this analysis with the results shown in Fig. 11 for each velocity model and equivalent stiffness. For velocity model A, it is clear the TF spectral ratios are quite different from the aftershock spectral ratios indicating the need for the stiffer bedrock layer at depth in Models B-E. It is possible that the trough in the computed SSR from 5 to 5.5 Hz for Models C-E is in part due to the stratigraphic/topographic effect at HCEA station. A similar response is observed in the recorded SSRs (HHMT/HCEA) in Fig. 11. Considering the response for the Models B-E, the theoretical spectral ratios tend to match the target spectral ratios better with the best fits coming from Models D and E. For Models D and E, the better performance is observed for the $Vs_{(TT)}$ and $Vs_{(SWM)}$ equations. In addition, the theoretical spectral ratio is only slightly different from the 1D transfer function ratio, which assumes a shear wave velocity of the bedrock equal to the equivalent velocity of the relief, $Vs_{(BR)}$.

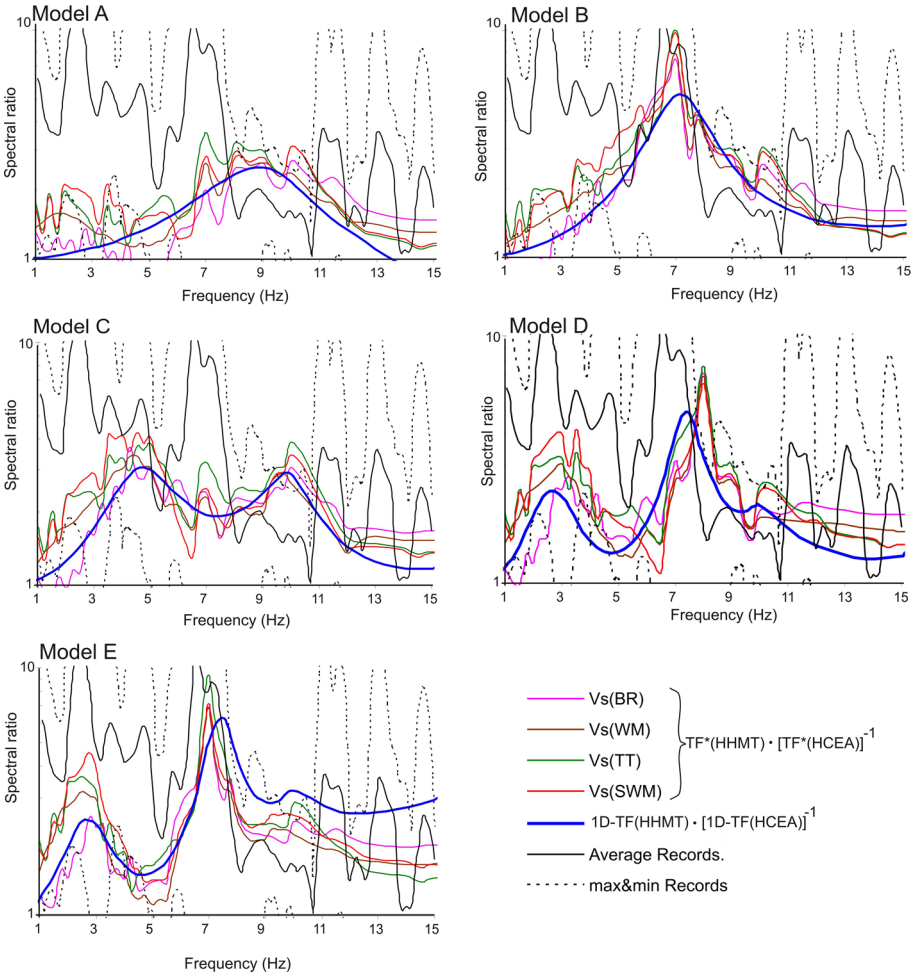

Fig. 11 Comparison between the aftershock spectral ratio and the transfer function spectral ratios for the HHMT Vs-depth models each in relation to the HCEA Vs-depth model, both for free field response (1D analysis) and topographic response (DEM surface). Aftershock spectral ratios obtained from Assimaki and Jeong (2013)

5 Conclusions

A reliability analysis was conduct using the metamodeling software SiSeRHMap by computing the topographic and/or stratigraphic effects associated with two previously well-documented topographic effects studies. The comparison analysis of the East Mountain area (Utah, USA) was performed using spectral ratios determined using the MRM and SSR methods from horizontal ground velocity records. The data-set was recorded using a dense array of broadband sensors located along a steep complex area of topography. Comparisons between the SiSeRHMap results and experimental results indicate that the SiSeRHMap results are more consistent with the MRM results as oppose to the SSR results, which agrees with findings from the Wood and Cox (2016) study. A

comparison of the spatial distribution of the spectral acceleration between the SiSeRHMap results and MRM results shows a general good agreement for the large number of the stations with a more consistent and robust agreement in the fundamental topographic frequency range. As expected, a poorer fit is observed at frequencies higher than the fundamental topographic frequency range. However, it is believed the response at higher frequencies is primarily due to 1D site effects, which were not modelled in this particular scenario by the SiSeRHMap model.

In general, topographic amplification were observed along the crest of the topographic features, but the largest amplification were observed at the outer edge of peninsula type sub-ridges, which are characterized by both a significant longitudinal and transverse curvature. For these locations, the SiSeRHMap results match the MRM results in the fundamental topographic frequency range very well for Station A3 with about a 5% difference. However, for the equivalent station in Line B (B2), a significant difference (100%) was observed between the two results with the MRM results indicating an amplification of approximately 5.0 for the station, while the SiSeRHMap results indicate an amplification around 2.5. Given the significant similarities between topographic features, the potential differences in the subsurface conditions at each station need to be investigated further to understand disagreement between the two stations. The best fit between the experimental and the SiSeRHMap results is observed at the main ridge location (A6-A8 and B5-B8) as well as along the slope and in the valley (Line V). These 2D ridge locations seem to less complex than the peninsula type features discussed previously.

For the comparison analysis conducted in the Port-au-Prince area, the recorded and computed spectral ratios from ground motion data at two crest recording stations, HHMT (Hotel Montana) and HCEA were compared. The stations are located at the crests of two ridge/peninsula type topographic features, which can be similar in 2D cross section, but have significant differences in their 3D geometric models. Specifically, the feature instrumented by the HHMT Station has much greater curvature values (i.e., steeper slopes) than the HCEA site. This difference in curvature manifests itself in the results as a substantial greater amplification peak for the HHMT station (more than 30%) than the HCEA station at the predominant topographic frequencies without considering the potential influence of lithology (i.e., no 1D site effects). When considering the stiffness of the subsurface materials, the seismic bedrock is encountered at a relative shallow depth for the HCEA station, while a weather bedrock formation was encountered at the HHMT site. This results in a difference in the 1D site effects frequency range at the two sites. Following other studies (Assimaki and Jeong 2013; Fleur et al. 2016), a parametric analysis was performed at the HHMT site in order to determine the most appropriate stiffness model for the site. In contrast to the East Mountain Study, the SiSeRHMap model was utilized in the coupled topographic and 1D site effects mode as shown in Fig. 1. The results of parametric analysis are as follows:

(1) the difference in the amplitude and frequency distribution from the topographic predictive model for the HCEA and HHMT sites makes it possible to define and verify the role of topographic effects in the site response for the HHMT site;
(2) results from the parametric analysis indicate the models with a stiff bedrock layer (Vs of 2300 m/s) below the weather rock layer at the HHMT site produce more realistic results for the site.

(3) the topographic effect predicted by the model is predominant with amplification about 2× for the frequency peak centred at 2.5–3 Hz, while the stratigraphic (1D site effects) effect mainly the peak near to 7 Hz.
(4) in the parametric analysis, the best performance was observed when considering an equivalent uniform relief having a shear wave velocity estimated based on the time-averaged shear wave velocity, $Vs_{(TT)}$ or the weighted harmonic mean shear wave velocity $Vs_{(SWM)}$.
(5) The acceleration response spectra, obtained by full stratigraphic topographic analysis performed by SiSeRMap, highlights the relative low amplification for the HCEA site, which verifies its use as an adequate reference site for SSR analysis in accordance with experimental evidence in Assimaki and Jeong (2013) and Fleur et al. (2016), even if this is not a flat site.

Overall, this study demonstrates the applicability and reliability of SiSeRHMap for estimating the effects of both stratigraphy and topography for real world 3D topographic features.

Acknowledgements We are grateful to anonymous reviewer #1 for providing comments on the manuscript. These comments and suggestions have improved the paper. We are grateful to Susan Hough (reviewer #2) for her precious comments and suggestions. Doubtless, her words have well defined the purpose and reliability of the model: *The "series parallel" approach represents a simplification of complex physics, but is otherwise sound and well-motivated*. We consider these words are an encouragement to continue in improving and extending the model.

References

Alfaro P, Delgado J, García-Tortosa FJ, Lenti L, López JA, López-Casado C, Martino S (2012) Widespread landslides induced by the Mw 5.1 earthquake of 11 May 2011 in Lorca, SE Spain Engineering Geology Volumes 137–138, 1 June 2012, pp 40–52

Arabasz WJ, Julander DR (1986) Geometry of seismically active faults and crustal deformation within the Basin and Range-Colorado Plateau transition in Utah. Geol Soc Am Spec Pap 208:43–74

Arabasz WJ, Ake J, McCarter MK, McGarr A, Nava SJ, Pankow KL (2002) Coal-mining seismicity in the Trail Mountain area, Utah: Part I¾ Case study for assessing ground-shaking hazard (abstract), Eos, Trans. Am. Geophys. Union 83 (47), Fall Meeting Suppl., Abstract S12A–1170

Ashford SA, Sitar N (1997) Analysis of topographic amplification of inclined shear waves in a steep coastal bluff. Bull Seismol Soc Am 87(3):692–700

Ashford SA, Sitar N (2002) Simplified method for evaluating seismic stability of steep slopes. J Geotech Geoenviron 128(2):119–129

Ashford SA, Sitar N, Lysmer J, Deng N (1997) Topographic effects on the seismic response of steep slopes. Bull Seismol Soc Am 7(3):701–709

Assimaki D, Gazetas G (2004) Soil and topographic amplification on canyon banks and the Athens 1999 earthquake. J Earthq Eng 8(1):1–44

Assimaki D, Jeong S (2013) Ground-motion observations at hotel Montana during the M 7.0 2010 Haiti earthquake: topography or soil amplification? Bull Seismol Soc Am 103(5):2577–2590

Assimaki D, Kausel E (2007) Modified topographic amplification factors for a single-faced slope due to kinematic soil-structure interaction. J Geotech Geoenviron Eng 133(11):1414–1431

Assimaki D, Gazetas G, Kausel E (2005a) Effects of local soil conditions on the topographic aggravation of seismic motion: parametric investigation and recorded field evidence from the 1999 Athens earthquake. Bull Seismol Soc Am 95(3):1059–1089

Assimaki D, Kausel E, Gazetas G (2005b) Soil-dependent topographic effects: a case study from the 1999 Athens earthquake. Earthq Spectra 21(4):929–966

Athanasopoulos GA, Pelekis PC, Leonidou EA (1999) Effects of surface topography on seismic ground response in the Egion (Greece) 15 June 1995 earthquake. Soil Dyn Earthq Eng 18:135–149

Barani S, Massa M, Lovati S, Spallarossa D (2014) Effects of surface topography on ground shaking prediction: implications for seismic hazard analysis and recommendations for seismic design. Geophys J Int 197:1551–1565

Bard PY (1982) Diffracted waves and displacement field over two-dimensional elevated topographies. Geophys J R Astr Soc 71:731–760

Bard PY, Tucker BE (1985) Ridge and tunnel effects: comparing observations with theory. Bull Seismol Soc Am 75:905–922

Boore DM (1973) The effect of simple topography on seismic waves: implications for the accelerations recorded at Pacoima Dam, San Fernando valley, California. Bull Seismol Soc Am 63(5):1603–1609

Bouchon M, Schultz CA, Toksoz MN (1996) Effect of threedimensional topography on seismic motion. J Geophys Res 101:5835–5846

Bouckovalas G, Papadimitriou A (2003) Multi-variable relations for soil effects on seismic ground motion. Earthq Eng Struct Dyn 32:1867–1896

Bouckovalas G, Papadimitriou A (2005) Numerical evaluation of slope topography effects on seismic ground motion. Soil Dyn Earthq Eng 25:547–558

Buech F, Davies TR, Pettina JR (2010) The little Red Hill seismic experimental study: topographic effects on ground motion at a bedrock-dominated mountain edifice. Bull Seismol Soc Am 100(5A):2219–2229

Castellani A, Chesi C, Peano A, Sardella L (1982) Seismic response of topographic irregularities. In: Cakmak AS, Abdel-Ghaffar AM, Brebbia CA (eds) Proceedings of soil dynamics and earthquake engineering conference, vol 1. A. A. Balkema, Rotterdam, pp 251–268

Cauzzi C, Faccioli E, Poggi V, Fäh D, Edwards B (2011) Prediction of long-period displacement response spectra for low-to-moderate seismicity regions: Merging the Swiss earthquake waveform archive with a global fully digital strong-motion dataset. In Fourth IASPEI/IAEE international symposium: effects of surface geology on seismic motion, University of California Santa Barbara, USA, Aug 2011

Chávez-García FJ, Sánchez LR, Hatzfeld D (1996) Topographic site effects and HVSR. A comparison between observations and theory. Bull Seismol Soc Am 86(5):1559–1573

Cox BR, Bachhuber J, Rathje E, Wood CM, Dulberg R, Kottke A, Green RA, Olson SM (2011) Shear wave velocity- and geology-based seismic microzonation of Port-au-Prince, Haiti. Earthq Spectra 27(S1):S67–S92

Fahjan YM, Özdemir Z (2008) Scaling of earthquake accelerograms for non-linear dynamics analyses to match the earthquake design spectra. In: The 14th world conference on earthquake engineering. October 12–17, 2008, Beijing, China

Fleur SS, Bertrand E, Courboulex F, de Lépinay BM, Deschamps A, Hough S, Cultrera G, Boisson D, Prépetit C (2016) Site effects in Port-au-Prince (Haiti) from the analysis of spectral ratio and numerical simulations. Bull Seismol Soc Am 106(3):1298–1315

Gazetas G, Kallou PV, Psarropoulos PN (2002) Topography and soil effects in the Ms 5.9 Parnitha (Athens) earthquake: the case of Adames. Nat Hazards 27(1–2):133–169

Geli L, Bard PY, Jullen B (1988) The effect of topography on earthquake ground motion: a review and new results. Bull Seismol Soc Am 78:42–63

Grelle G, Guadagno FM (2013) Regression analysis for seismic slope instability based on double phase viscoplastic sliding model of the rigid block. Landslides 5:583–597

Grelle G, Revellino P, Guadagno FM (2011) Methodology for seismic and post-seismic stability assessing of natural clay slope based on a visco-plastic behavioural model in simplified dynamic analysis. Soil Dyn Earthq Eng 12:1248–1260

Grelle G, Bonito L, Revellino P, Guerriero L, Guadagno FM (2014) A hybrid model for mapping simplified seismic response via a GIS-metamodel approach. Nat Hazards Earth Syst Sci 14:1703–1718

Grelle G, Bonito L, Lampasi A, Revellino P, Guerriero L, Sappa G, Guadagno FM (2016a) SiSeRHMap v1.0: a simulator for mapped seismic response using a hybrid model. Geosci Model Dev 9:1567–1596

Grelle G, Bonito L, Revellino P, Sappa G (2016b) Frequency-dependent topographic seismic amplification by a "gray box model" using GIS morphometric data Rend. Online Soc Geol It 41(2016):342–345

Hancilar U, Çaktı E, Erdik M, Franco GE, Deodatis G (2014) Earthquake vulnerability of school buildings: probabilistic structural fragility analyses. Soil Dyn Earthq Eng 67(2014):169–178

Hartzell S, Carver DL, King KW (1994) Initial investigation of site and topographic effects at Robinwood Ridge, California. Bull Seismol Soc Am 84(5):1336–1349

Hartzell S, Meremonte M, Ramírez-Guzmán L, McNamara D (2014) Ground motion in the presence of complex topography: earthquake and ambient noise sources. Bull Seismol Soc Am 104(1):451–466

Hough SE, Altidor JR, Anglade D, Given D, Janvier MG, Maharrey JZ, Meremonte M, Mildor BS-L, Prepetit C, Yong A (2010) Localized damage caused by topographic amplification during the 2010 M7.0 Haiti earthquake. Nat Geosci 3:778–782

Hough SE, Yong A, Altidor JR, Anglade D, Given D, Mildor S-L (2011) Site characterization and site response in Port-au-Prince, Haiti. Earthq Spectra 27(S1):S137–S155
Idriss IM, Seed HB (1967) Response of earthbanks during earthquakes. J Soil Mech Found Div ASCE 93(SM3):61–82
Iwahashi J, Pike RJ (2007) Automated classifications of topography from DEMs by an unsupervised nested-means algorithm and a three-part geometric signature. Geomorphology 86:409–440
Jafarzadeh F, Shahrabi MM, Jahromi HF (2015) On the role of topographic amplification in seismic slope instabilities. J Rock Mech Geotech Eng 7(2):163–170
Klein FW (1978) Hypocenter location program HYPOINVERSE, U.S. Geol. Surv. Open-File 29 Rept. 78–694, 113 pp
Kovacs WD, Seed HB, Idriss IM (1971) Studies of seismic response of clay banks. J Soil Mech Found Div ASCE 97(SM2):441–455
Le Brun B, Hatzfeld D, Bard P-Y (1999) Experimental study of the ground-motion on a large scale topographic hill a Kitherion (Greece). J Seismol 3:1–15
Lee WHK, White RA, DH Harlow, Rogers JA, Spudich P, Dodge DA (1994) Digital seismograms of selected aftershocks of the Northridge earthquake recorded by a dense seismic array on February 11, 1994 at Cedar Hill Nursery in Tarzana, California, U.S. Geol Surv Open-File Rept. 94–234
Massa M, Lovati S, D'Alema E, Ferretti G, Bakavoli M (2010) An experimental approach for estimating seismic amplification effects at the top of a ridge, and the implication for groundmotion predictions: the case of Narni, Central Italy. B Seismol Soc Am 100:3020–3034
Massa M, Lovati S, Franceschina G, D'Alema E, Marzorati S, Mazza S, Cattaneo M, Selvaggi G, Amato A, Michelini A, Augliera P (2014) ISMD, a web portal for real-time processing and dissemination of INGV strong-motion data. Seismol Res Lett 85(4):863–877
Maufroy E, Cruz-Atienza VM, Gaffet S (2012) A Robust Method for Assessing 3-D Topographic Site Effects: a Case Study at the LSBB Underground Laboratory. France Earthq Spectra 28(3):1097–1115
Maufroy E, Cruz Atienza VM, Cotton F, Gaffet S (2015) Frequency scaled curvature as a proxy for topographic site effect amplification and ground motion variability. B Seismol Soc Am 105:354–367
May TW (1980) The effectiveness of trenches and scarps in reducing seismic energy, Ph.D. Thesis, University of California at Berkeley, Berkeley, California
Ohtsuki A, Harumi K (1983) Effect of topography and subsurface inhomogeneities on seismic SV waves. Earthq Eng Struct Dyn 11:441–462
Özel NM, Harmandar E, Pinar A (2011) Sensitivity of the strong ground motion time histories to a finite source model: a case study for the January 12, 2010 Haiti earthquake (Mw = 7.0). Soil Dyn Earthq Eng 31(11):1441–1451
Paolucci R (2002) Amplification of earthquake ground motion by steep topographic irregularities. Earthq Eng Struct Dyn 31:1831–1853
Paolucci R, Faccioli E, Maggio F (1999) 3D Response analysis of an instrumented hill at Matsuzaki, Japan, by a spectral method. J Seismol 3:191–209
Pechmann JC, Arabasz WJ, Pankow KL, Burlacu R, McCarter MK (2008) Seismological report on the 6 August 2007 Crandall Canyon Mine collapse in Utah. Seismol Res Lett 79(5):620–636
Rai M, Rodriguez-Marek A, Yong A (2016) An empirical model to predict topographic effects in strong ground motion using California small-to medium-magnitude earthquake database. Earthq Spectra 32(2):1033–1054
Rathje EM, Bachhuber J, Dulberg R, Cox BR, Kottke A, Wood CM, Green RA, Olson S, Wells D, Rix G (2011) Damage patterns in Port-au-Prince during the 2010 Haiti Earthquake. Earthq Spectra 27(S1):S117–S136
Sànchez-Sesma FJ (1985) Diffraction of elastic SH waves by wedges. Bull Seismol Soc Am 75:1435–1446
Sanò T, Pugliese A (1999) Parametric study on topographic effect in seismic soil amplification. In: Oliveto G, Brebbia CA (eds) Proceeding of advances in earthquake engineering, earthquake resistance engineering structure II, vol 4. WIT Press, Southampton, pp 321–330
Sitar N, Clough GW, Bachus R (1980) Behavior of weakly cemented soil slopes under static and seismic loading, Report No. 44, The John A. Blume Earthquake Engineering Center, Stanford University
Spudich P (1996) Directional topographic site response at Tarzana observed in aftershocks of the 1994 Northridge, California, Earthquake: Implications for mainshock motions. Bull Seismol Soc Am 86:193–208
Terrier M, Bialkowski A, Nachbaur A, Prépetit C, Joseph YF (2014) Revision of the geological context of the Port-au-Prince metropolitan area, Haiti: implications for slope failures and seismic hazard assessment. Nat Hazards Earth Syst Sci 14(9):2577–2587
Torgoev A, Havenith HB (2016) 2D dynamic studies combined with the surface curvature analysis to predict Arias Intensity amplification. J Seismol 20(3):711–731

Trifunac MD, Hudson DE (1971) Analysis of the Pacoima dam accelerogram—San Fernando, California, earthquake of 1971. Bull Seismol Soc Am 61(5):1393–1411

Williams DJ, Arabasz WJ (1989) Mining-related and tectonic seismicity in the East Mountain Area Wasatch Plateau, Utah. Pageoph 129:345–368

Wong IG (1993) Tectonic stresses in mine seismicity: are they significant? In: Young RP (ed) Rockbursts and Seismicity in Mines 93. A. A. Balkema, Rotterdam, pp 273–278

Wood CM (2013) Field investigation of topographic effects using mine seismicity. Ph.D. Dissertation, Dept. of Civil, Architectural, and Environmental Engineering, University of Texas, Austin, TX, 377 pg

Wood CM, Cox BR (2015) Experimental data set of mining-induced seismicity for studies of full-scale topographic effects. Earthq Spectra 31(1):541–564

Wood CM, Cox BR (2016) Comparison of field data processing methods for the evaluation of topographic effects. Earthq Spectra 32(4):2127–2147

Zimmaro P, Stewart JP (2016) Engineering reconnaissance following the 2016 M 6.0 Central Italy Earthquake. Version 1 Geotechnical Extreme Events Reconnaissance Association (Report No. GEER-050) Dated: 15 September 2016